# The microstructures of metallic materials from additive manufacturing

Charles-André Gandin

# Solidification microstructures from additive manufacturing processes

**Charles-André GANDIN**

*Centre de Mise en Forme des Matériaux, Mines ParisTech, Sophia Antipolis, UMR CNRS 7635, France*

## 1.1. Solidification microstructures from additive manufacturing processes

The principles defining the formation of solidification structures in wide growth rate and temperature gradient ranges, typical of additive manufacturing processes, are discussed here. The generated microstructures only rarely represent the thermodynamic equilibrium. They are the result of competitions between nucleation and growth of phases in unsteady mass and energy transfer regimes. However, at the solid-liquid interface, thermodynamic equilibrium can be preserved. In cases of extreme velocities where it is not, solute trapping comes into play, complicating the explanation of microstructural morphologies and their phase and solute compositions.

### 1.1.1. *Introduction*

Solidification is present in additive manufacturing processes involving a melting step. This is the case for powder bed fusion (PBF) processes using a heat source (L-PBF: laser beam, E-PBF: electron beam), fusion processes with a projected powder (DED: Direct Energy Deposition), for example using a laser source (LMD: Laser Metal Deposition), or processes for depositing material by electric arc wire fusion (WAAM: Wire Arc Additive manufacturing). These technologies are described in Chapter 1 of Volume 1.

The formation of a solid can occur below a characteristic temperature of thermodynamic equilibrium. For an alloy of composition $w_0$, this temperature is called the liquidus, $T_L^{\alpha l}$. It coincides with the eutectic temperature, $T_E^{\alpha\beta l}$, when the composition approaches that of the eutectic, $w_E^{\alpha\beta l}$. The size of the microstructure is strongly dependent on the temperature gradient, $G$, and the solidification rate, $V_s$, prevailing at the solid-liquid interface during growth. Thus, the primary, $\lambda_1$, et secondary, $\lambda_2$, dendritic spacings, and the eutectic interlamellar spacing, $\lambda_e$, follow the following trends (Dantzig and Rappaz 2016):

$$\lambda_1 \propto G^{-1/2} V_s^{-1/4} \quad [1.1]$$

$$\lambda_2 \propto G^{-1/3} V_s^{-1/3} \quad [1.2]$$

$$\lambda_e \propto V_s^{-1/2} \quad [1.3]$$

A first estimate of $G$ and $V_s$ can be based on isotherms $T_L^{\alpha l}$ and $T_E^{\alpha\beta l}$. Moreover, in the case of directional growth, called columnar growth, the orientation of the microstructure can also be approximated by that of the temperature gradient. These first elements indicate the importance of the analysis of heat transfers to understand and control the solidification microstructures.

---

Section 1.1 written by Charles-André Gandin.

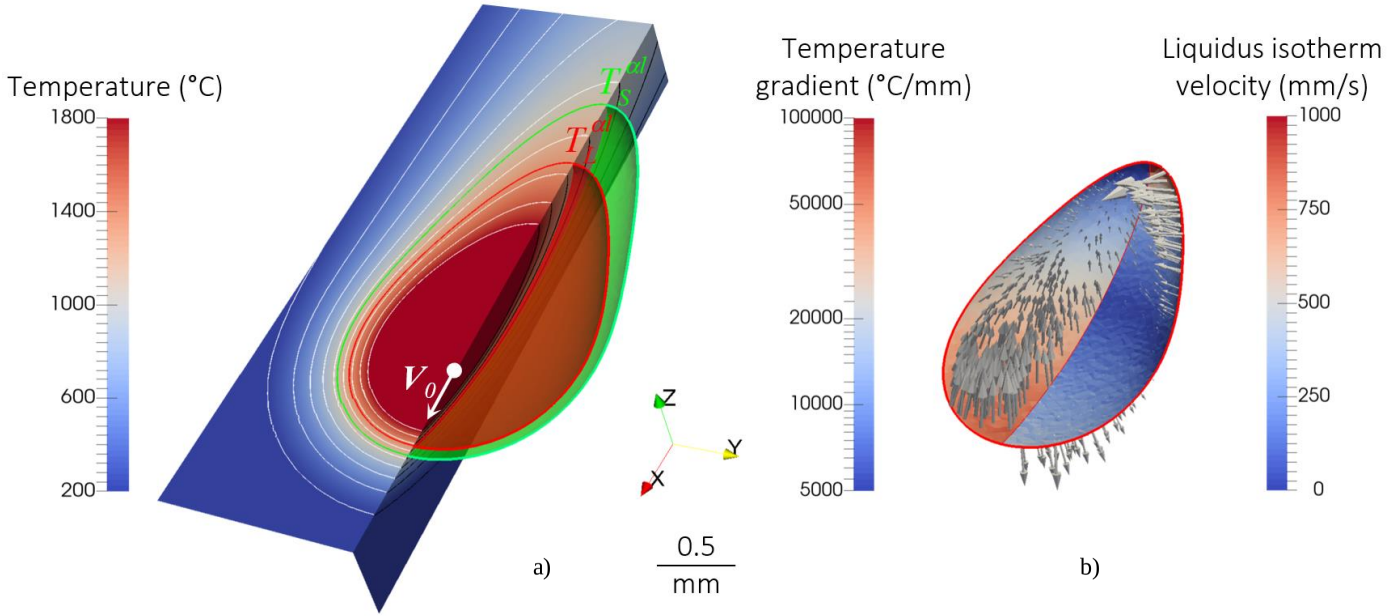


**Figure 1.3.** *Distributions a) of the temperature, b) of the temperature gradient and of the velocity of the isotherm of the liquidus of the alloy, $T_L^{al}$ (red surfaces and contours), representative of the diffusion of heat in a metallic material during an additive manufacturing process using a moving speed heat source $V_0$*

COMMENTS ON FIGURE 1.3.– *The melting of the material generates a melt-pool in the region of temperature above* $T_L^{al}$ *and a mushy zone, i.e. mixture of solid and liquid phases, between* $T_L^{al}$ *and the solidus isotherm of the alloy, (a), green surface and contour). Material: Inconel 718 with* $T_L^{al}$ *= 1337 °C and* $T_S^{al}$ *= 1075 °C, according to (Antonsson et Fredriksson 2005) ; thermal diffusivity,* $a_{th} = 10^{-5}\ m^2\ s^{-1}$*, thermal conductivity,* $K = 30\ W\ m^{-1}\ K^{-1}$*, initial temperature,* $T_0 = 20$ *°C. Heat source according to the model of (Cline and Anthony 1977): power,* $P_0 = 100$ *W, standard deviation of the Gaussian representing the spatial distribution of energy around the center of the heat source,* $10^{-4}$ *m, velocity,* $V_0 = 1\ m\ s^{-1}$*. The central position of the heat source is represented by the white dot on the surface of the weld-pool.*

Figure 1.3 gives an illustration of a temperature field generating a liquid pool by melting a metallic material according to the model of Cline and Anthony. The material is characterized by its thermal diffusivity, $a_{th}$, its thermal conductivity, $K$, and its initial temperature, $T_0$. The heat source moves linearly at the speed $V_0$. It is also described by its power, $P_0$, and its spatial Gaussian distribution of energy with the standard deviation representing here the diameter of the source. The temperature field at instant t is then given by an analytical formula. Other analytical forms exist, such as the solution of (Rosenthal 1946), a simplified version of the solution of Cline and Anthony for a point heat source (i.e., zero standard deviation). The limitations of these solutions are numerous: purely stationary regimes, absence of the effect of convective transport and movements of the liquid-gas interface, constant properties with temperature, etc. Numerical modeling is therefore relevant in this context, as evidenced by chapter 4 of volume 1. However, the orders of magnitude given in figure 1.3 are sufficient to realize the variations in $G$ and $V_s$ and, as a result of using the equations [1.1] to [1.3], variations in microstructure size and orientation. In front of the heat source, the isotherm velocities $T_L^{\alpha l}$ shown in Figure 1.3 come out of the weld-pool, which represents the propagation of heat in the cold material, i.e., fusion. Conversely, behind the heat source, the isotherm of the liquidus propagates towards the weld-pool already formed, indicating its cooling and therefore its solidification. Obviously, it is the region downstream from the heat source that interests us for the study of the formation of solidification microstructures. In this region, going up from the bottom of the weld-pool towards its upper surface behind the heat source, we also observe that $G$ decreases as $V_s$ increases. The ratio $G/V_s$ is therefore high at the bottom of the bath and low at its upper surface. This evolution is indicative of a columnar directional growth, from the bottom of the weld-pool, whereas an equiaxed growth is possible at the surface of the weld-pool (Hunt 1984). These analyzes can be summarized in maps representing domains of $G$ and $V_s$ in which columnar and equiaxed microstructures are found (Kurz and Fisher 1998; Dantzig and Rappaz 2009) (example in figure 1.2).

Given the speed and temperature gradient domains involved, the rest of this section describes a series of phenomena explaining the formation of solidified microstructures in additive manufacturing processes, including high speed solidification. The following concepts will be introduced: growth kinetics and morphologies of microstructures, thermodynamic equilibrium of the interface, competition of growth between microstructures and selection of grain structures. We will limit ourselves to dendritic and eutectic structures, omnipresent in the transformations of metallic alloys from a liquid.

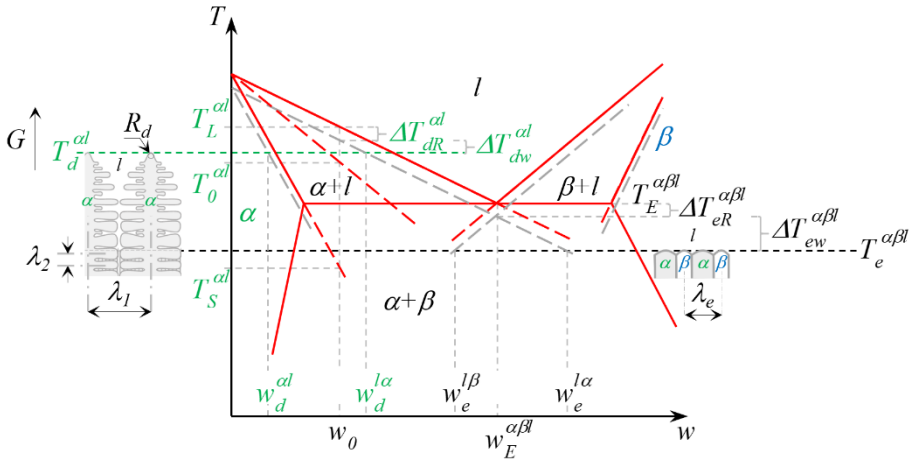


**Figure 1.4.** *Schematic representations (center) of a phase diagram for a binary mixture and of the dendritic (left) and eutectic (right) microstructures growing in a temperature gradient, G, with indication of the temperatures, lengths, curvature undercooling, chemical undercooling and characteristic chemical compositions.*

COMMENTS ON FIGURE 1.4.– *The dashed lines schematize the equilibria in the presence of a curvature (in grey) and the $T_0$ lines (in red) (see text). The effects of solidification rate on the modification of thermodynamic equilibria are not included here.*

### 1.1.2. *Growth kinetics with local interface equilibrium*

The literature is rich in works explaining the kinetics and morphologies of solidification microstructures. We limit ourselves below to the case of binary alloys. In addition, we consider dilute alloys and a linearized representation of the phase diagram, as schematized in figure 1.4: the slopes of the boundaries between single-phase liquid, *l*, crystalline solid domains, $\alpha$ and $\beta$, and bi-phasic, $\alpha + l$, $\beta + l$ and $\alpha + \beta$, are constant. For the alloy with composition $w_0$ at temperature $T$ such that the solid $\alpha$ and liquid phases coexist, of

respective solute chemical compositions $w^{\alpha l}$ and $w^{l\alpha}$, the thermodynamic equilibrium of the mixture is characterized by the partition coefficient $k^{\alpha l} = w^{\alpha l} / w^{l\alpha}$. In the example in figure 1.4, $w^{\alpha l} < w^{l\alpha}$ in the biphasic domain $\alpha + l$, so that $k^{\alpha l} < 1$ at the interface between the solid $\alpha$ and the liquid, reflecting the chemical segregation of the solute in the liquid from the interface $\alpha l$. When the solid $\alpha$ is growing at the rate $V_s$, the solute will then accumulate in the liquid at the solid-liquid interface. Similarly, although the temperature can be deemed constant at the interface, the energy of the solid is lower than that of the liquid which, during solidification, releases heat. These segregated quantities, solute and energy, will have to be evacuated by diffusion in the liquid. Moreover, when the interface $\alpha l$ is not planar, its curvature adds an undercooling proportional to the interfacial energy. Diffusive and curvature phenomena generate a deviation from the thermodynamic equilibrium which is represented in Figure 1.4 by undercooling $\Delta T_d^{\alpha l} = T_L^{\alpha l} - T_d^{\alpha l}$ and $\Delta T_e^{\alpha l} = T_E^{\alpha\beta l} - T_e^{\alpha\beta l}$, where $T_d^{\alpha l}$ and $T_e^{\alpha\beta l}$ are respectively the growth temperatures of the $\alpha$ dendritic and $\alpha + \beta$ eutectic microstructures. We observe in figure 1.4 that the eutectic structure is interdendritic, that is to say that it grows in the residual liquid with a composition close to the eutectic, $w_E^{\alpha\beta l}$, due to the accumulation of the solute rejected at the interface $\alpha l$ during dendritic growth. In directional growth, i.e., in a temperature gradient $G$, the growth fronts are thus below the equilibrium temperatures $T_L^{\alpha l}$ and $T_E^{\alpha\beta l}$. This situation is encountered in additive manufacturing where $G/V_s$ is high, $V_s$ can then be estimated using the velocity of isotherms $T_L^{\alpha l}$ and $T_E^{\alpha\beta l}$ deduced from the overall energy balance carried out at the process level (figure 1.3). In general, and without going into the details that can be found in several reference works (Kurz and Fisher 1989), growth undercooling is written as the sum of several contributions (energy diffusion is neglected here because very often in additive manufacturing a columnar constrained growth is observed):

$$\Delta T_d^{\alpha l} = -m^{l\alpha} w_0 \left( \frac{(1 - k^{\alpha l})\mathrm{Iv}(\mathrm{Pe}_w)}{1 - (1 - k^{\alpha l})\mathrm{Iv}(\mathrm{Pe}_w)} \right) + \frac{2\Gamma^{\alpha l}}{R_d} \qquad [1.4]$$

$$\Delta T_e^{\alpha\beta l} = A_w \, Pe_{\lambda_e} + A_R / \lambda_e \qquad [1.5]$$

The first contribution of equation [1.4] is the undercooling of chemical origin, $\Delta T_{d,w}^{\alpha,l} = -m^{l\alpha}\left(w_d^{l\alpha} - w_0\right)$, related to the diffusion of the solute in the liquid. It is estimated by the product of the slope of the liquidus of the phase diagram, $m^{l\alpha}$, and the gap between the composition far from the interface, $w_0$, and the composition of the liquid at the interface, $w_d^{\alpha l} = w_0 \left(1 - (1 - k^{\alpha l})\mathrm{Iv}(\mathrm{Pe}_w)\right)^{-1}$. The latter is given by the Ivantsov solution $\mathrm{Iv}(\mathrm{Pe}_w)$ of the steady diffusion profile of the solute in the liquid for a value of the Peclet number, $\mathrm{Pe}_w = (R_d \, V_s) / (2 \, D^l)$, where $R_d$ is the radius of the parabolic tip representative of the dendritic growth shape and $D^l$ is the chemical diffusion coefficient

of the solute in the liquid. The second contribution of equation [1.4] is that of the curvature at the tip of the dendrite, $\Delta T_{dR}^{\alpha l} = 2\Gamma^{\alpha l}/R_d$, being the Gibbs Thomson coefficient. As for equation [1.5], it is also the sum of a chemical undercooling, $\Delta T_{ew}^{\alpha\beta l} = A_w\, Pe_{\lambda_e}$, and a curvature undercooling, $\Delta T_{eR}^{\alpha\beta l} = A_R\,/\lambda_e$, with $Pe_{\lambda_e} = (\lambda_e V_s)/D^l$ the Péclet number associated with the eutectic interlamellar spacing $\lambda_e = (A_R/A_w)^{1/2}(D^l/V_s)^{1/2}$ this expression justifying the equation [1.3]. The coefficients $A_R$ and $A_w$ are defined by the properties of the phase diagram and physicochemical properties such as the Gibbs-Thomson coefficients between the solid and liquid phases, $\alpha l$ and $\beta l$ (Kurz and Fisher 1989; Dantzig and Rappaz 2016).

However, if the growth rate is not too high, the solid-liquid interface can be considered to be at equilibrium, i.e., its compositions can always be read on the equilibrium phase diagram in the presence of a curvature of the interface. The equilibrium diagram then remains the basic tool to work from. The diagram with curvature is preferential to that without curvature because it always represents a thermodynamic equilibrium where the free energy of the solid phase accounts for its curvature. Note also that the curvature of the interface certainly modifies the thermodynamic equilibrium, but independently of the speed of the interface.

### 1.1.3. *Loss of local interface equilibrium at high solidification rates*

The contributions above express the solute diffusion effects as well as that of the curvature of the interface. In doing so, they always assume that the interface is in thermodynamic equilibrium. When the solid is growing in the liquid at the rate $V_s$, we have seen that the interface is the site of solute exchanges between the solid and liquid phases. To maintain a constant value of the partition coefficient, equal to that read on the phase diagram, the atoms will need time to be evacuated from the interface zone by diffusion in the liquid. It is this assumption that is made to develop the models given by equations [1.4] and [1.5]. The interface is then always at local thermodynamic equilibrium, despite the equilibrium deviations linked to the solute diffusion fluxes as well as to the curvature. To do this, the diffusion length of the atoms in the liquid, $D^l/V_s$, must be much larger than the thickness of the interface, $\delta$, where $D^l$ represents the diffusion coefficient of the solute in the liquid. This condition can be written:

$$\mathrm{Pe}_\delta << 1 \text{ with } \mathrm{Pe}_\delta = \delta V_s / D^l \qquad [1.6]$$

where $\mathrm{Pe}_\delta$ represents the dimensionless Peclet number, ratio of variables $\delta$ and $D^l/V_s$. In practice, for a rough (also called diffuse) interface representative of most metal alloys, $\delta$ is around a few atomic layers ($10^{-9}$ m). The diffusion coefficient in the liquid is approximately $10^{-9}$ m$^2$ s$^{-1}$, the deviation from this interface thermodynamic equilibrium condition takes place for velocities close to 1 m s$^{-1}$. To translate the deviation from the

thermodynamic equilibrium of the interface as a function of the solidification rate, (Aziz 1982) introduce an effective partition coefficient, $k_v^{\alpha l}$, function of the Peclet number, $\mathrm{Pe}_\delta$:

$$k_v^{\alpha l} = \frac{k^{\alpha l} + Pe_\delta}{1 + Pe_\delta} \quad [1.7]$$

Doing so, when $\mathrm{Pe}_\delta$ is low enough, the effective partition coefficient tends towards that of equilibrium $k^{\alpha l}$. On the other hand, for sufficiently high values of $\mathrm{Pe}_\delta$, $k_v^{\alpha l}$ tends towards 1, which reflects "solute trapping" or the absence of chemical redistribution at the interface. The solid-liquid interface is then no longer in thermodynamic equilibrium. By extension, it is also proposed to modify the slope of the liquidus of the equilibrium phase diagram, $m^{l\alpha}$, to account for the speed of the interface (Boettinger and Coriell 1986):

$$m_v^{l\alpha} = m^{l\alpha}\left(1 + \frac{k^{\alpha l} - k_v^{\alpha l}(1 + \ln(k^{\alpha l}/k_v^{\alpha l}))}{1 - k^{\alpha l}}\right) \quad [1.8]$$

The chemical undercooling is then given by $-m_v^{l\alpha}(w_d^{l\alpha} - w_0)$. Again, at low speed, $m_v^{l\alpha}$ tends towards $m^{l\alpha}$, the value at equilibrium. If the equations [1.7] and [1.8] propose a model of evolution of the thermodynamic properties to describe the partition of the solute at the interface according to the rate of solidification, they do not give the unique value towards which the chemical composition must tend for a sufficiently high speed. It is the analysis of (Baker and Cahn 1971) that provides the necessary construction. The thermodynamic equilibrium condition given by the equality of chemical potentials, $\mu^l = \mu^\alpha$, is replaced by a condition on the free enthalpy of the phases, $G^l = G^\alpha$. The first case corresponds to the common tangent of curves $G^l$ and $G^\alpha$ at temperature $T$ and pressure $p$ of the mixture. It provides access to the equilibrium compositions of the phases, $w^{\alpha l}$ and $w^{l\alpha}$, and therefore at value $k^{\alpha l}$, thus constructing the phase diagram in figure 1.4. The second case more simply look forthe composition at which the free enthalpies of the phases are equal at temperature $T$ of the mixture, thus corresponding to the solute trapping condition. Conversely, one can investigate at what temperature an alloy of known composition can give rise to solidification without segregation between the solid and liquid phases. In a phase diagram, this temperature is sometimes referred to as the line $T_0$ (Kurz and Fisher 1989; Dantzig and Rappaz 2016). It is shown in the two-phase domain $\alpha + l$ in figure 1.4.

Another phenomenon giving rise to a deviation from thermodynamic equilibrium is the attachment kinetics of atoms. It designates the capacity of the atoms of the liquid to reorganize to join a growing $\alpha$ solid phase. To quantify it, we introduce a kinetic undercooling, $\Delta T_{dc}^{\alpha l}$, inversely proportional to the speed of the solid-liquid interface:

$$\Delta T_{dc}^{\alpha l} = V_s/\mu_k \quad [1.9]$$

where $\mu_k = (\Delta S_f V_{son}) / (R T_f)$ is the kinetic attachment coefficient with $R$ the ideal gas constant, $T_f$ is the melting point of the pure body, $\Delta S_f$ is the entropy of fusion and $V_{son}$ is the speed of sound (around 1000 m $s^{-1}$) (Turnbull 1962). For a metal with a rough interface, $\mu_k$ is around $10^3$ m $s^{-1}$ $K^{-1}$. Solid growth rates of the order of 1 m $s^{-1}$ are required for attachment kinetic undercooling to play a role. In fact, at extreme speeds (100 to 1000 m $s^{-1}$), some systems also show that the atoms no longer have time to reorganize at the interface to form a crystal. The atoms of the liquid freeze and a glassy phase can be observed.

Figure 1.5 gives an illustration of the temperature of a dendritic structure, $T_d^{\alpha l}$, calculated using equations [1.4], [1.7], [1.8] and [1.9]. Note that the model covers both dendritic and cellular morphologies, i.e., dendritic without secondary branches. We also see that additional morphologies are mentioned, flat front and banded, which we will now introduce.

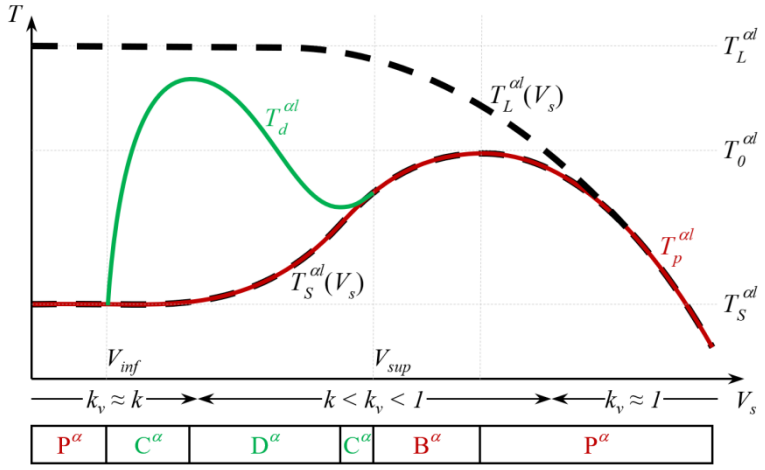


**Figure 1.5.** *Growth temperature of a solid-liquid interface as a function of its velocity $V_s$ for flat interface morphology, $T_p^{\alpha l}$ (in red), and cellular or dendritic, $T_d^{\alpha l}$ (in green)*

COMMENTS ON FIGURE 1.5.– *The schematic representation is given here for an alloy of known composition, the solid at the interface consisting of a single phase and the growth being directional in a fixed temperature gradient (recomposed from (Gremaud 1990)). The identified morphologies are planar (P), cellular (C), dendritic (D) and banded (B).*

### 1.1.4. *Growth morphologies*

Speed limits exist, which define the morphologies of the microstructures. Mullins and Sekerka (Mullins and Sekerka 1964) establish a stability analysis of a flat front $\alpha l$. The expression for this limit is $V_{inf} = G\,D^l / \Delta T_0$, where $\Delta T_0 = T_L^{\alpha l} - T_S^{\alpha l}$ is the solidification interval of the alloy defined by the thermodynamic equilibrium temperature values at the start and end of solidification, considering only the two-phase equilibrium $\alpha + l$. This speed corresponds to the constitutional undercooling limit (Tiller *et al.* 1953) for which the flat front can only grow stationary at the solidus of the alloy, $T_S^{\alpha l}$, the temperature gradient at the interface, $G$, being higher than its chemical counterpart, $m^{l\alpha} G_w^{l\alpha}$, where $G_w^{l\alpha}$ represents the composition gradient of the solute in the liquid at the interface $\alpha l$.

Considering the orders of magnitude typical for metal alloys and additive manufacturing processes, $\Delta T_0 = 100$ K, $G = 10^5$ K m$^{-1}$, and $D^l = 10^{-9}$ m$^2$ s$^{-1}$, we obtain $V_{inf} = 10^{-6}$ m s$^{-1}$. Considering the velocity field represented in figure 1.3, we do not expect to meet this condition of existence of the flat front in additive manufacturing. Indeed, even if the speed at the bottom of the pool starts from zero, it increases very rapidly to reach several millimeters per second only a few micrometers behind the heat source. This speed limit, $V_{inf}$, below which growth morphology is flat, $P^\alpha$, is represented in figure 1.5.

For a higher solidification rate, the morphology becomes cellular, $C^\alpha$, then dendritic, $D^\alpha$, the latter corresponding to the diagrams of figures 1.1 and 1.4. For even higher speeds, the interface $\alpha l$ gradually re-stabilizes, resuming a cellular morphology, $C^\alpha$, then flat front, $P^\alpha$. This is the limit of absolute stability at high speed. Again, an analytic expression can be derived, $V_{sup} = (D^l \Delta T_0) / (k^{\alpha l} \Gamma^{\alpha l})$. It is interesting to note the absence of the temperature gradient in this expression, as well as the presence of the Gibbs-Thomson coefficient reflecting the effect of the interfacial energy. It is indeed this energy which stabilizes the interface perturbations at high solidification rates. By taking typical values of the properties previously introduced, and adding $\Gamma^{\alpha l} = 2 \cdot 10^{-7}$ K m and $k^{\alpha l} = 0.5$, we obtain $V_{sup} = 1$ m s$^{-1}$. Thus, in areas of beads where the liquidus isotherm is the fastest, it could be that this limit is reached. Moreover, this was the order of magnitude used in microstructures studies produced by laser remelting in the 1990s, giving rise to the observation of the transition $C^\alpha - P^\alpha$ at high solidification rates (Kurz and Trivedi 1996). In figure 1.5, it can also be noted that a growth regime in the form of banded microstructure, $B^\alpha$, is encountered close to the stability of the flat front $V_{sup}$ (Kurz and Trivedi 1996). Its explanation requires the effects of non-equilibrium growth of the interface to be accounted for. Generally speaking, it is close to this speed $V_{sup}$ that the effects of deviation from thermodynamic equilibrium are present in metallic alloys. Beyond a certain speed, the crystalline phase $\alpha$ can no longer form and the liquid is frozen

in the form of a metallic glass. This is observed for powder atomization or roller quenching processes and the speeds here are estimated to be around 100 m $s^{-1}$ (Dantzig and Rappaz 2016).

The temperature of a flat front, $T_p^{\alpha l}$, can also be calculated as a function of the solidification rate. Since the growth of the flat front in steady state can only be achieved at the solidus of the alloy, $T_p^{\alpha l} = T_S^{\alpha l}$, its undercooling $\Delta T_p^{\alpha l}$ is the sum of the chemical contribution, $\Delta T_{pw}^{\alpha l} = m_v^{l\alpha}\left(w_p^{l\alpha} - w_0\right)$ where $w_p^{l\alpha} = w_0/k_v^{\alpha l}$ is the composition of the liquid at the solidus temperature, plus the kinetic contribution given by equation [1.9].

For a rate less than $V_{inf}$, that is to say a low rate, $k_v^{\alpha l} = k^{\alpha l}$, $m_v^{\alpha l} = m^{\alpha l}$ and $V_s/\mu_k$ is negligible, so that $\Delta T_p^{\alpha l} = \Delta T_0$ corresponding to growth at the solidus temperature. By increasing the speed, the solidus is affected, $T_S^{\alpha l}\left(V_s\right)$, as shown in figure 1.5. We note that the liquidus temperature is also affected and that it is only at very high rates that $T_L^{\alpha l}\left(V_s\right)$ and $T_S^{\alpha l}\left(V_s\right)$ are close to $T_0$, with $k_v^{\alpha l}$ tending towards 1. But, as illustrated in figure 1.5, the kinetic undercooling contribution is already present before $T_L^{\alpha l} = T_S^{\alpha l} = T_0$ and the temperature of the flat front continues to decrease. Complete solute trapping only takes place for a rate that has exceeded the absolute stability velocity, $V_{sup}$. The curves describing the cellular/dendritic and flat front structures in Figure 1.5 naturally meet at the stability limits of the flat front. The selected structure is the one with the highest growth temperature and therefore requires the lowest equilibrium deviation. The stability regimes of the structures expected as a function of the speed are then listed, in ascending order: $P^{\alpha}$, $C^{\alpha}$, $D^{\alpha}$, $C^{\alpha}$, $B^{\alpha}$ and $P^{\alpha}$.

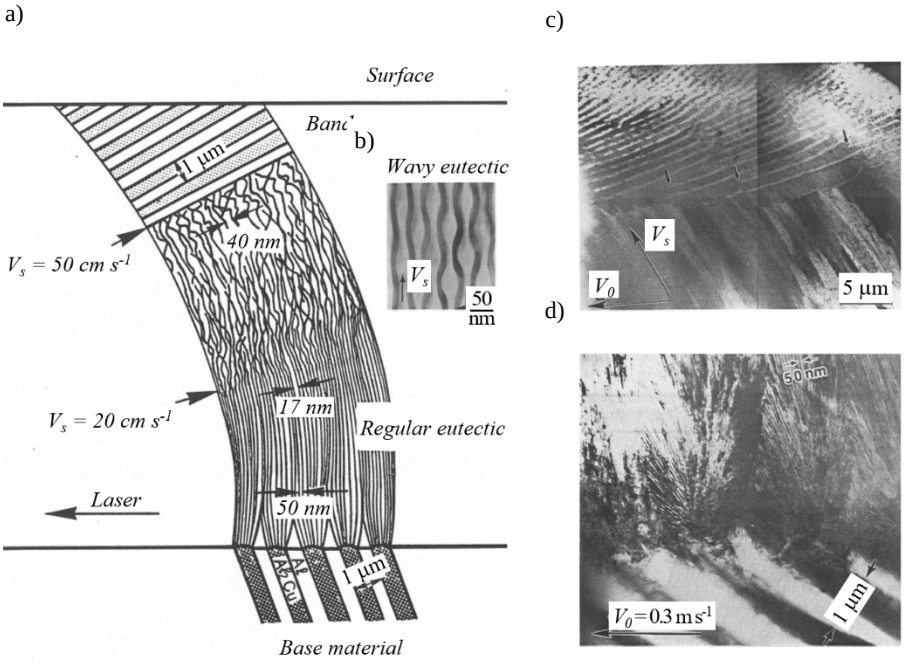


**Figure 1.6.** *Solidification structures of an alloy of eutectic composition Al – 33 %pds Cu observed in a longitudinal cross section XZ*

COMMENTS ON FIGURE 1.6.– *See reference figure 1.3. Structures in the center of a laser trace showing a) a schematic representation of the microstructural evolutions from the unmelted base material to the upper metal surface, of the regular (d) and wavy (b) eutectic and the transition to a band structure (c), according to (Zimmermann 1990).*

Figure 1.6 gives a summary of the evolution of the structures observed for an alloy of eutectic composition Al – 33 wt% Cu (Zimmermann 1990). Although the growth theories are different from those of dendritic microstructures, we find the schematic description of the role velocity on the microstructures as the solidification of the pool occurs. We note in particular the decrease in the size of the interlamellar spacing observed in equation [1.3] and the transition to a banded structure at high rates. In fact, chemical contributions, curvature and kinetics are also at the origin of these evolutions. It should be noted, however, that the structure described for the single-phase microstructure growing in the liquid close to the absolute stability limit is replaced by a coarser wavy eutectic structure.

### 1.1.5. *Growth competition between microstructures*

Figures 1.5 and 1.6 introduced and illustrated the principles of growth competition during the solidification of an alloy. They must be supplemented by the possible competition between different types of microstructures.

Thus, we see in Figure 1.4 that the diagram shows, for the same alloy of composition $w_0$, both a dendritic structure and a eutectic structure. The figure suggests that $T_d^{\alpha l} > T_e^{\alpha\beta l}$ This situation is a special case because it is also possible to find, for the same alloy composition, situations for which $T_d^{\alpha l} < T_e^{\alpha\beta l}$. This can happen by changing the rate of solidification. In this case, the eutectic structure $\alpha + \beta$ developing at a temperature higher than that of the single-phase dendritic structure $\alpha$, the latter will be prevented from growing. In Figure 1.4, this principle can be extended to competition with a $\beta l$ structure, so that a total of three types of structures can compete. Depending on the growth conditions, the microstructure selected will not be the one with the highest equilibrium phase onset temperature, but rather the one with the highest growth temperature. It should be noted here that the same principle is applied in Figure 1.5 to establish which of the growth morphologies of an $\alpha l$ interface is selected.

Figure 1.7 schematizes the construction using the same phase diagram as in Figure 1.4 in a simplified way and for the composition alloy $w_0$. The growth temperatures of the microstructures resulting from the equilibria $\alpha l$, $\beta l$ and $\alpha\beta l$ are calculated as a function of the rate and transferred to the right. The upper part of the figure indicates which of the microstructures are the most stable on the basis of the criterion of the maximum growth temperature. It is thus found that at very low growth rates, it is a eutectic structure which is favored. This result is not intuitive, but corresponds to the fact that the $\alpha$ structure of the flat front grows at a much lower temperature defined by the solidus of the mixture $\alpha l$ at composition $w_0$, below the eutectic growth temperature. This lower limit is of little interest for additive manufacturing as mentioned above.

On the other hand, while the microstructure resulting from the single-phase interface $\alpha l$ is present in a wide range of rates in figure 1.7, the eutectic microstructure then a microstructure from the $\beta l$ interface become stable again at higher rates. For the alloy considered, it is then possible to plot on the phase diagram the domains of microstructure formation according to the rate of solidification. The procedure carried out over the entire composition range defines the coupled zone, i.e., the region of the phase diagram where only the eutectic structure appears, but also the regions where the single-phase primary phases $\alpha$ and $\beta$ are formed. It should be noted that the method described only applies to determining the structure growing at the highest temperature, called the primary solidification structure, without predicting the secondary phases formed from the liquid state, such as the inter-dendritic eutectic structure illustrated in figure 1.4.

Figure 1.7 therefore identifies the regions of composition and rate allowing the formation of one type of primary microstructure. By extension is constructed the microstructure selection map, such as in the Al-Fe system (Gilgien *et al.* 1995) and Al-Cu (Gill and Kurz 1995) for wide rate and chemical composition ranges. Maps and studies of competition between microstructures also exist in more limited domains for Ni-Al (Hunziker and Kurz 1999; Tourret *et al.* 2011) or Fe-Ni (Hunziker *et al.* 1998; Vandyoussefi *et al.* 2000; Dobler *et al.* 2004), including in particular peritectic microstructures, as well as for some multi-component systems.

In the presentation given, the phase diagram used is that at equilibrium, with domain limits that can be modified by the kinetic contribution via equations [1.8] and [1.9]. However, many systems present equilibria with metastable phases that must also be considered to determine any possible competing microstructures. There are many examples in the literature. The best known is probably that of the Fe-C diagram. While the stable eutectic of the phase diagram is defined by grey cast iron, composed of lamellae of a solid solution of iron, austenite, and graphite (composed of pure C), it is common to observe the formation of white cast iron, a metastable eutectic material with the same austenitic phase but also with the $Fe_3C$ intermetallic phase. The microstructure selection map must then focus on calculating the growth temperature of the metastable eutectic (austenite + $Fe_3C$), even though the intermetallic is not initially present in the equilibrium phase diagram. The stable and metastable phase diagrams must therefore be used to plot the growth temperature curves in Figure 1.7. The nucleation phase kinetics have not been considered here either. We confined ourselves to comparing growth temperatures assuming that the phases are already present or can germinate as soon as their thermodynamic equilibrium temperature is reached. Otherwise, nucleation must be added to the mechanisms governing the competition between microstructures. Finally, it should also be mentioned that the theories concerning growth competition between microstructures are mainly developed for binary model alloys. Extensions are necessary for application to industrial alloys.

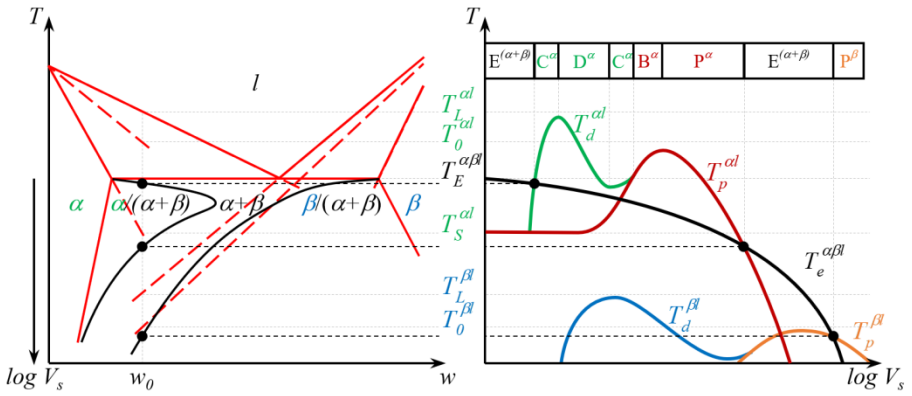


**Figure 1.7.** *Principle of the coupled zone in the case of a binary eutectic system*

COMMENTS ON FIGURE 1.7.– *For the alloy with composition $w_0$, the single-phase solidification microstructures $\alpha$ and $\beta$ can form as well as the eutectic two-phase structure $\alpha + \beta$. On the right, the growth temperatures of these three structures are plotted against velocity using growth kinetics models (e.g., equations [1.4] and [1.5]). The structure adopting the highest growth temperature is assumed to be the most stable, defining domains of existence according to the growth rate (according to (Kurz and Fisher 1989; Dantzig and Rappaz 2016)).*

### 1.1.6. *Selection of grain structures*

So far, we have considered the microstructure. The primary grain structure, or primary solidification macrostructure, is defined on a larger scale. It results from the growth of the primary microstructure which can be dendritic or eutectic according to the principle of selection seen in section 1.1.5. The grain is generally defined as the domain grouping together the microstructure resulting from the same germ. When the microstructure growth is by successive branches of the crystal, a relative uniformity of the crystallographic orientation of the microstructure within the same grain can exist. Similarly, in additive manufacturing where remelting and solidification alternate to build the part layer after layer, the crystallographic orientation can be propagated in the direction of the temperature gradient. The grain structures can then reach very large dimensions, close to those of the manufactured part in the direction of manufacture (i.e., the temperature gradient). Figure 1.1 shows the growth of dendritic grains developing in a liquid subjected to a temperature gradient $G$, cooling evenly at the rate $G \cdot V_L$ with $V_L$ the velocity of the liquidus isotherm. Three grains, numbered 1 to 3, are each composed of two dendrites of the same color. For these grains, the color corresponds to a

crystallographic orientation, here defined by a simple rotation $\theta$ with respect to the direction of the temperature gradient. The directions of the trunks and arms of dendrites of the same grain are therefore identical, generally oriented in the <100> crystallographic direction in the case of materials with a cubic dendritic microstructure. Also shown in Figure 1.1 are the distances between the liquidus isotherm of the alloy and the tip of the columnar dendrites. In steady state growth, the velocity $V_{s,0}$ of dendrites in grain 1, with orientation $\theta = 0°$, is equal to the isotherm velocity, $V_L$. The dendrites are located on isotherm $\Delta T_{\theta=0°}$, at a distance $\Delta z_{\theta=0°} = \Delta T_{\theta=0°} / G$ of the liquidus isotherm of the alloy. In the case of a grain with orientation $\theta \neq 0°$, such as grain 2 at the center of figure, so that a stationary growth is established, allowing the solidification front to follow the displacement of the isotherms at the rate $V_L$, the distance to travel in direction <100> is greater than for $\theta = 0°$. The speed in direction <100> is therefore greater, i.e., $V_{s,\theta\neq 0°} = V_L / \cos\theta$. As seen previously for a dendritic microstructure, a greater undercooling corresponds to a higher rate, $\Delta T_{\theta\neq 0°} > \Delta T_{\theta=0°}$, and therefore a greater distance $\Delta z_{\theta\neq 0°} = \Delta T_{\theta\neq 0°} / G > \Delta z_{\theta=0°}$. As a result, the tips of the grain 2 dendrites are geometrically blocked in their progression by the dendrite arms of grain 1. Blocking phenomena occur at the interfaces between the grains, in particular between grains 2 and 3. However, the consequence of these competitions leads to the progressive elimination of the grains disoriented with respect to the temperature gradient (high $\theta$ values), thus creating a crystallographic texture <100> aligned with the temperature gradient (low $\theta$ values).

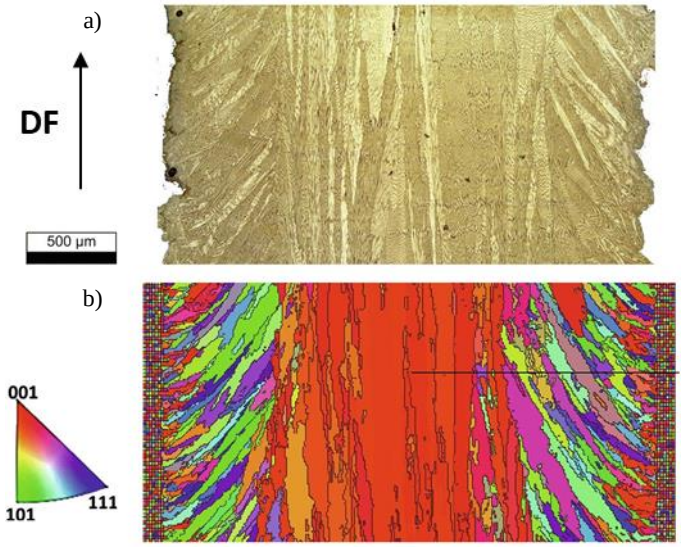


**Figure 1.8.** *Section of a sample produced by E-PBF from a CMSX-4 nickel base superalloy powder revealing a) the columnar grain structure (metallography) and b) the*

*associated strong texture (simulation), the direction of projection of the crystallographic orientations being vertical, corresponding with the direction of construction.*

COMMENTS ON FIGURE 1.8.– *Power and speed of the electron beam, $P_0$ = 300 W and $V_0$ = 0.5 m $s^{-1}$, preheat temperature, $T_i$ = 900 °C, thickness of successive deposits, 50 µm, according to (Koepf et al. 2019).*

Figure 1.8 provides an example of a columnar grain structure obtained by E-PBF for a nickel-based superalloy (Koepf *et al.* 2019) and its modeling using the cellular automata method (Gandin and Rappaz 1997; Carozzani *et al.* 2013). Particular attention to the metallographic cross section makes it possible to distinguish about ten layers built from bottom to top. It is the manufacture method implemented and the parameters of the process which allowed the growth of columnar grains by epitaxy. The simulation combines a three-dimensional description of the thermal process (for example figure 1.3) with a spatial description in the form of cells whose state (liquid or belonging to the microstructure) and crystallographic orientation evolve over time. To do this, the kinetics of the primary solidification microstructure (i.e., dendritic here) is integrated over time, proportionally to the undercooling defined by the temperature field and the equation [1.4]. It should be noted that, despite the velocity of the heat source used, no effects due to modification of the thermodynamic equilibrium is accounted for (equations [1.7] and [1.8]). Similarly, the dendritic growth kinetics is not coupled with the calculation of the multicomponent phase diagram and its properties. Finally, the coupling between the temperature fields and the development of the microstructure is weak, i.e., temperature is only used to calculate the grain structure without the structure itself influencing the temperature fields. The comparison is nevertheless remarkable and the method can also give rise to comparisons with pole figures or maps characterizing the crystallographic orientations and relationships between grains (Chen *et al.* 2016; Pineau *et al.* 2020).

The columnar growth competition explained above assumes that no new grain appears in the liquid. The origin of such columnar grains can be from nucleation in the undercooled liquid, at the undercooling $\Delta T_N$, as shown in figure 1.1, at a distance $\Delta z_N = \Delta T_N / G$. The equiaxed structure can then grow and end up blocking the growth of columnar grains, causing the columnar to equiaxed transition (CET). It should be noted that the origin of the equiaxed grains can also be the fragmentation or partial refusion of the existing dendritic microstructure and transport by convection of the fragments in front of the columnar growth front. The directions of the arms of the equiaxed grains are random. The simplest CET criterion is based on the integration of the growth kinetics of the envelopes of the equiaxed grains, with velocity $V_s(\Delta T)$, assuming a constant cooling rate, $G \cdot V_L$. The grains, although growing, are immobile, so that their undercooling $\Delta T$ only increases during cooling. By doing so, their size may be sufficient to mechanically halt the growth of columnar grains (Hunt 1984). Integration between nucleation positions

$\Delta z_N$ and the columnar front easily shows that the CET is a function of the ratio $G/V_s$ and nucleation undercooling, $\Delta T_N$, but also the growth kinetics of the dendrites and the density of the equiaxed grains. Other columnar to equiaxed transition criteria exist to account for fragmentation (Gandin 2000), solutal interaction between columnar and equiaxed dendrites (Martorano *et al.* 2003) and transport of equiaxed grains in the liquid (Leriche *et al.* 2015).

### 1.1.7. *Solidification in additive manufacturing*

The previous sections provide an overview of the phenomena occurring during the formation of solidification microstructures in additive manufacturing processes. We can resume several points.

– Firstly, the dendritic and eutectic microstructures can be described by the temperature field by considering the speed of the liquidus isotherm of the alloy and the temperature gradient in the liquid on this same isotherm.

– Theories for the kinetics of microstructures date back to the 1980s and 1990s. They concern the morphologies of the solid-liquid interfaces resulting from the growth of a single-phase or two-phase solid, mainly for binary metal alloys and single remelting passes of the material.

– The effects at high solidification rates are pertinent for metallic alloys only when the growth speed typically approaches 1 m $s^{-1}$. This speed is encountered in the upper part of the melt pool. Given the multilayer nature of the deposits made in additive manufacturing, leading to a systematic remelting of the previously deposited layers, it is not easy to know if these conditions can be encountered on the microstructures finally formed, unless only being interested by the last solidified layers. Further microstructural analysis of the beads is required. It would require conditions allowing the formation of microstructures typical of rapid solidification, after one and several layers, and associated simulations.

– The coupling of theories with a complete description of thermodynamic equilibria remains to be systematized, which has begun (Gilgien 1996; Senninger e*t al.* 2018). This is necessary to allow a more direct application to multi-component alloys.

– Simulating the grain structures results from the calculation of the microstructure kinetics. Therefore, work on grain structures directly depends on work done on microstructures. The advantage of grain structure modeling is to provide the crystallographic orientation field and the grain size, information not available from a simple theoretical analysis of the kinetics of micro-structures.

### 1.1.8. *Acknowledgements*

The author expresses his thanks to Théophile Camus, Gildas Guillemot and Oriane Senninger for their contributions to this section.

## 1.7. Bibliography

Aboulkhair, N.T., Everitt, N.M., Ashcroft, I., Tuck, C. (2014). Reducing porosity in AlSi10Mg parts processed by selective laser melting. *Additive Manufacturing*, 1/4, 77–86.

Alnajjar, M., Christien, F., Wolski, K., Bosch, C. (2019). Evidence of austenite by-passing in a stainless steel obtained from laser melting additive manufacturing. *Additive Manufacturing*, 25, 187–195.

Andreau, O., Koutiri, I., Peyre, P., Penot, J.-D., Saintier, N., Pessard, E., De Terris, T., Dupuy, C., Baudin, T. (2019). Texture control of 316L parts by modulation of the melt pool morphology in selective laser melting. *Journal of Materials Processing Technology*, 264, 21–31.

Andrews, K.C. (1965). Empirical formulae for the calculation of some transformation temperatures. *Journal of the Iron and Steel Institute*, 203, 721–727.

Antonsson, T., Fredriksson, H. (2005). The effect of cooling rate on the solidification of INCONEL 718. *Metallurgical and Materials Transactions B*, 36(1), 85–96.

Aziz, M.J. (1982). Model for solute redistribution during rapid solidification. *Journal of Applied Physics*, 53(2), 1158–1168.

Bai, J.Y., Yang, C.L., Lin, S.B., Dong, B.L., Fan, C.L. (2015). Mechanical properties of 2219-Al components produced by additive manufacturing with TIG. *Int. J. Adv. Manuf. Technol.*, 86(1/4), 479–485.

Baker, J.C., Cahn, J.W. (1971). The Thermodynamics of Solidification, Seminar series on Solidification. Rapport, ASM, Novelty, 23–58.

Bidron, G., Doghri, A., Malot, T., Fournier-dit-Chabert, F., Thomas, M., Peyre, P. (2020). Reduction of the hot cracking sensitivity of CM-247LC superalloy processed by laser cladding using induction preheating. *Journal of Materials Processing Technology*, 277, 116461.

Boettinger, W.J., Coriell, S.R. (1986). Microstructure Formation in Rapidly Solidified Alloys. Dans *Science and Technology of the Undercooled Melt*, Sahm, P.R., Jones, H., Adam, C.M. (dir.). Springer Netherlands, Dordrecht, 81–109 [En ligne]. Disponi-ble à l'adresse : http://link.springer.com/10.1007/978-94-009-4456-5_5 [Consulté le 3 novembre 2020].

Boswell, J.H., Clark, D., Li, W., Attallah, M.M. (2019). Cracking during thermal post-processing of laser powder bed fabricated CM247LC Ni-superalloy. *Materials & Design*, 174, 107793.

Carluccio, D., Bermingham, M.J., Zhang, Y., StJohn, D.H., Yang, K., Rometsch, P.A., Wu, X., Dargusch, M.S. (2018). Grain refinement of laser remelted Al-7Si and 6061 aluminium alloys with Tibor® and scandium additions. *Journal of Manufacturing Processes*, 35, 715–720.

Carozzani, T., Gandin, C.-A., Digonnet, H., Bellet, M., Zaidat, K., Fautrelle, Y. (2013). Direct Simulation of a Solidification Benchmark Experiment. *Metallurgical and Materials Transactions A*, 44(2), 873–887.

Carter, L.N., Martin, C., Withers, P.J., Attallah, M.M. (2014). The influence of the laser scan strategy on grain structure and cracking behaviour in SLM powder-bed fabricated nickel superalloy. *Journal of Alloys and Compounds*, 615, 338–347.

Casati, R., Coduri, M., Riccio, M., Rizzi, A., Vedani, M. (2019). Development of a high strength Al–Zn–Si–Mg–Cu alloy for selective laser melting. *Journal of Alloys and Compounds*, 801, 243–253.

Catchpole-Smith, S., Aboulkhair, N., Parry, L., Tuck, C., Ashcroft, I.A., Clare, A. (2017). Fractal scan strategies for selective laser melting of 'unweldable' nickel superalloys. *Additive Manufacturing*, 15, 113–122.

Chauvet, E., Kontis, P., Jägle, E.A., Gault, B., Raabe, D., Tassin, C., Blandin, J.-J., Dendievel, R., Vayre, B., Abed, S., Martin, G. (2018). Hot cracking mechanism affecting a non-weldable Ni-based superalloy produced by selective electron Beam Melting. *Acta Materialia*, 142, 82–94.

Chen, B., Moon, S.K., Yao, X., Bi, G., Shen, J., Umeda, J., Kondoh, K. (2017). Strength and strain hardening of a selective laser melted AlSi10Mg alloy. *Scripta Materialia*, 141, 45–49.

Chen, S., Guillemot, G., Gandin, C.-A. (2016). Three-dimensional cellular automaton-finite element modeling of solidification grain structures for arc-welding processes. *Acta Materialia*, 115, 448–467.

Cline, H.E., Anthony, T.R. (1977). Heat treating and melting material with a scanning laser or electron beam. *Journal of Applied Physics*, 48(9), 3895–3900.

Cloots, M., Uggowitzer, P.J., Wegener, K. (2016). Investigations on the microstructure and crack formation of IN738LC samples processed by selective laser melting using Gaussian and doughnut profiles. *Materials & Design*, 89, 770–784.

Cong, B., Ding, J., Williams, S.W. (2014). Effect of arc mode in cold metal transfer process on porosity of additively manufactured Al-6.3%Cu alloy. *The International Journal of Advanced Manufacturing Technology*, 76(9/12), 1593–1606.

Dantzig, J.A., Rappaz, M. (2009). *Solidification*, 1re édition. EPFL Press, Lausanne.

Davis, J.R. (1997). *ASM Speciality Handbook: Heat Resistant Material*. ASM International, Almere.

De Terris, T. (2019). Fabrication additive par fusion laser sélective (SLM) d'un superalliage base nickel : relations procédé-microstructures-propriétés mécaniques. Thèse de doctorat, École nationale supérieure d'arts et métiers, Paris.

DebRoy, T., Wei, H.L., Zuback, J.S., Mukherjee, T., Elmer, J.W., Milewski, J.O., Beese, A.M., Wilson-Heid, A., De, A., Zhang, W. (2018). Additive manufacturing of metallic components – Process, structure and properties. *Progress in Materials Science*, 92, 112–224.

Dehoff, R.R., Kirka, M.M., Sames, W.J., Bilheux, H., Tremsin, A.S., Lowe, L.E., Babu, S.S. (2015). Site specific control of crystallographic grain orientation through electron beam additive manufacturing. *Materials Science and Technology*, 31(8), 931–938.

Deirmina, F., Peghini, N., AlMangour, B., Grzesiak, D., Pellizzari, M. (2019). Heat treatment and properties of a hot work tool steel fabricated by additive manufacturing. *Materials Science and Engineering: A*, 753, 109–121.

Delroisse, P., Jacques, P.J., Maire, E., Rigo, O., Simar, A. (2017). Effect of strut orientation on the microstructure heterogeneities in AlSi10Mg lattices processed by selective laser melting. *Scripta Materialia*, 141, 32–35.

Dinda, G.P., Dasgupta, A.K., Mazumder, J. (2012). Evolution of microstructure in laser deposited Al–11.28%Si alloy. *Surface and Coatings Technology*, 206(8/9), 2152–2160.

Dobler, S., Lo, T.S., Plapp, M., Karma, A., Kurz, W. (2004). Peritectic coupled growth. *Acta Materialia*, 52(9), 2795–2808.

Doghri, A. (2019). Vers une maîtrise de la réparation par le procédé CLAD de pièces aéronautiques en Inconel 738 LC : compréhensions des mécanismes de fissuration et modélisations associées. Thèse de doctorat, Université de Lorraine, Nancy.

Dong, H.B. (2007). Analysis of Grain Selection during Directional Solidification of Gas Turbine Blades. Dans *World Congress on Engineering*. IAENG, Londres, 4–9.

Du, R., Gao, Q., Wu, S., Lü, S., Zhou, X. (2018). Influence of TiB2 particles on aging behavior of in-situ TiB2/Al-4.5Cu composites. *Materials Science and Engineering: A*, 721, 244–250.

Dubourg, L., Ursescu, D., Hlawka, F., Cornet, A. (2005). Laser cladding of MMC coatings on aluminium substrate: influence of composition and microstructure on mechanical properties. *Wear*, 258(11/12), 1745–1754.

DuPont, J.N., Notis, M.R., Marder, A.R., Robino, C.V., Michael, J.R. (1998). Solidification of Nb-bearing superalloys: Part I. Reaction sequences. *Metallurgical and Materials Transactions A*, 29(11), 2785–2796.

Elmer, J.W., Allen, S.M., Eagar, T.W. (1989). Microstructural development during solidification of stainless steel alloys. *Metallurgical Transactions A*, 20(10), 2117–2131.

Facchini, L., Vicente, N., Lonardelli, I., Magalini, E., Robotti, P., Molinari, A. (2010). Metastable Austenite in 17-4 Precipitation-Hardening Stainless Steel Produced by Selective Laser Melting. *Advanced Engineering Materials*, 12(3), 184–188.

de Formanoir, C., Michotte, S., Rigo, O., Germain, L., Godet, S. (2016). Electron beam melted Ti–6Al–4V: Microstructure, texture and mechanical behavior of the as-built and heat-treated material. *Materials Science and Engineering: A*, 652, 105–119.

Gale, W.F., Totemeier, T.C. (2004). *Smithells Metals Reference Book*, 8e édition. Elsevier Butterworth-Heinemann, Oxford.

Gandin, C.-A. (2000). From constrained to unconstrained growth during directional solidification. *Acta Materialia*, 48(10), 2483–2501.

Gilgien, P., Zryd, A., Kurz, W. (1995). Microstructure selection maps for Al-Fe alloys. *Acta Metallurgica et Materialia*, 43(9), 3477–3487.

Gill, S.C., Kurz, W. (1995). Rapidly solidified AlCu alloys—II. Calculation of the microstructure selection map. *Acta Metallurgica et Materialia*, 43(1), 139–151.

Gong, X., Lydon, J., Cooper, K., Chou, K. (2014). Beam speed effects on Ti-6Al-4V microstructures in electron beam additive manufacturing. *Journal of Materials Research*, 29(17), 1951–1959.

Gremaud, M. (1990). Solidification rapide : étude microstructurale des alliages Al-Fe après refusion superficielle par laser. Thèse de doctorat, EPFL, Lausanne.

Gu, J., Ding, J., Cong, B., Bai, J., Gu, H., Williams, S.W., Zhai, Y. (2014). The Influence of Wire Properties on the Quality and Performance of Wire+Arc Additive Manufactured Aluminium Parts. *Advanced Materials Research*, 1081, 210–214.

Gu, J., Ding, J., Williams, S.W., Gu, H., Ma, P., Zhai, Y. (2016a). The effect of inter-layer cold working and post-deposition heat treatment on porosity in additively manufactured aluminum alloys. *Journal of Materials Processing Technology*, 230, 26–34.

Gu, J., Ding, J., Williams, S.W., Gu, H., Bai, J., Zhai, Y., Ma, P. (2016b). The strengthening effect of inter-layer cold working and post-deposition heat treatment on the additively manufactured Al–6.3Cu alloy. *Journal of Materials Processing Technology*, 230, 26–34.

Gu, J., Wang, X., Bai, J., Ding, J., Williams, S., Zhai, Y., Liu, K. (2018). Deformation microstructures and strengthening mechanisms for the wire+arc additively manufactured Al-Mg4.5Mn alloy with inter-layer rolling. *Materials Science and Engineering A*, 712, 292–301.

Guraya, T., Singamneni, S., Chen, Z.W. (2019). Microstructure formed during selective laser melting of IN738LC in keyhole mode. *Journal of Alloys and Compounds*, 792, 151–160.

Haldar, B., Saha, P. (2018). Identifying defects and problems in laser cladding and suggestions of some remedies for the same. *Materials Today: Proceedings*, 5(5), 13090–13101.

Hann, D.B., Iammi, J., Folkes, J. (2011). A simple methodology for predicting laser-weld properties from material and laser parameters. *Journal of Physics D: Applied Physics*, 44(44), 445401.

Hosseini, E., Popovich, V.A. (2019). A review of mechanical properties of additively manufactured Inconel 718. *Additive Manufacturing*, 30, 100877.

Hunt, J.D. (1984). Steady state columnar and equiaxed growth of dendrites and eutectic. *Materials Science and Engineering*, 65(1), 75–83.

Hunziker, O., Kurz, W. (1999). Directional solidification and phase equilibria in the Ni-Al system. *Metallurgical and Materials Transactions A*, 30(12), 3167–3175.

Hunziker, O., Vandyoussefi, M., Kurz, W. (1998). Phase and microstructure selection in peritectic alloys close to the limit of constitutional undercooling. *Acta Materialia*, 46(18), 6325–6336.

Jägle, E., Sheng, Z., Kürnsteiner, P., Ocylok, S., Weisheit, A., Raabe, D. (2016). Comparison of Maraging Steel Micro- and Nanostructure Produced Conventionally and by Laser Additive Manufacturing. *Materials*, 10(1), 8.

Kempen, K., Yasa, E., Thijs, L., Kruth, J.-P., Van Humbeeck, J. (2011). Microstructure and mechanical properties of Selective Laser Melted 18Ni-300 steel. *Physics Procedia*, 12, 255–263.

Koepf, J.A., Soldner, D., Ramsperger, M., Mergheim, J., Markl, M., Körner, C. (2019). Numerical microstructure prediction by a coupled finite element cellular automaton model for selective electron beam melting. *Computational Materials Science*, 162, 148–155.

Körner, C., Helmer, H., Bauereiß, A. (2014). *Tailoring the grain structure of IN718 during selective electron beam melting.* EDP Sciences, Les Ulis.

Kou, S. (2003). *Welding Metallurgy*, 2e édition. John Wiley, New York.

Kreitcberg, A., Brailovski, V., Turenne, S. (2017). Effect of heat treatment and hot isostatic pressing on the microstructure and mechanical properties of Inconel 625 alloy processed by laser powder bed fusion. *Materials Science and Engineering: A*, 689, 1–10.

Kurz, W., Fisher, D.J. (1998). *Fundamentals of solidification*, 4e édition. Trans Tech Publications, Uetikon-Zurich.

Kurz, W., Trivedi, R. (1996). Banded solidification microstructures. *Metallurgical and Materials Transactions A*, 27(3), 625–634.

Lei, Z., Bi, J., Chen, Y., Chen, X., Qin, X., Tian, Z. (2019). Effect of energy density on formability, microstructure and micro-hardness of selective laser melted Sc- and Zr-modified 7075 aluminum alloy. *Powder Technology*, 356, 594–606.

Leriche, N., Combeau, H., Gandin, C.-A., Založnik, M. (2015). Modelling of Columnar-to-Equiaxed and Equiaxed-to-Columnar Transitions in Ingots Using a Multiphase Model. *IOP Conference Series: Materials Science and Engineering*, 84, 012087.

Liu, X., Zhao, C., Zhou, X., Shen, Z., Liu, W. (2019). Microstructure of selective laser melted AlSi10Mg alloy. *Materials & Design*, 168, 107677.

Maisonneuve, J. (2008). Fabrication directe de pièces aéronautiques en TA6V et IN718 : projection et fusion sélective par laser. Thèse de doctorat, École nationale supérieure des Mines de Paris, Paris.

Marchese, G., Lorusso, M., Parizia, S., Bassini, E., Lee, J.-W., Calignano, F., Manfredi, D., Terner, M., Hong, H.-U., Ugues, D., Lombardi, M., Biamino, S. (2018). Influence of heat treatments on microstructure evolution and mechanical properties of Inconel 625 processed by laser powder bed fusion. *Materials Science and Engineering: A*, 729, 64–75.

Martin, J.H., Yahata, B.D., Hundley, J.M., Mayer, J.A., Schaedler, T.A., Pollock, T.M. (2017). 3D printing of high-strength aluminium alloys. *Nature*, 549(7672), 365–369.

Martina, F., Williams, S.W., Colegrove, P. (2013). Improved microstructure and increased mechanical properties of additive manufacture produced Ti-6Al-4V by interpass cold rolling. Dans *SFF symposium*. NSF, Austin, 490–496.

Martorano, M.A., Beckermann, C., Gandin, C.-A. (2003). A solutal interaction mechanism for the columnar-to-equiaxed transition in alloy solidification. *Metallurgical and Materials Transactions A*, 34(8), 1657–1674.

Montero-Sistiaga, M.L., Mertens, R., Vrancken, B., Wang, X., Van Hooreweder, B., Kruth, J.-P., Van Humbeeck, J. (2016). Changing the alloy composition of Al7075 for better processability by selective laser melting. *Journal of Materials Processing Technology*, 238, 437–445.

Mullins, W.W., Sekerka, R.F. (1964). Stability of a Planar Interface During Solidifi-cation of a Dilute Binary Alloy. *Journal of Applied Physics*, 35(2), 444–451.

Murr, L.E., Gaytan, S.M., Ramirez, D.A., Martinez, E., Hernandez, J., Amato, K.N., Shindo, P.W., Medina, F.R., Wicker, R.B. (2012). Metal Fabrication by Additive Manufacturing Using Laser and Electron Beam Melting Technologies. *Journal of Materials Science & Technology*, 28(1), 1–14.

Ojo, O.A., Richards, N.L., Chatuverdi, M.C. (2006). Study of the fusion zone and heat-affected zone microstructures in tungsten inert gas-welded Inconel 738LC superal-loy. *Metallurgical and Materials Transactions A: Physical Metallurgy and Materials Science*, 37(2), 421–433.

Parimi, L.L., Ravi, G.A., Clark, D., Attallah, M.M. (2014). Microstructural and texture development in direct laser fabricated IN718. *Materials Characterization*, 89, 102–111.

Pineau, A., Guillemot, G., Reinhart, G., Regula, G., Mangelinck-Noël, N., Gandin, C.-A. (2020). Three-dimensional cellular automaton modeling of silicon crystallization with grains in twin relationships. *Acta Materialia*, 191, 230–244.

Pinter, Z. (2017). Study of wire + arc additive manufacturing. Thèse de doctorat, Université de Cranfield, Cranfield.

Pröbstle, M., Neumeier, S., Hopfenmüller, J., Freund, L.P., Niendorf, T., Schwarze, D., Göken, M. (2016). Superior creep strength of a nickel-based superalloy produced by selective laser melting. *Materials Science and Engineering: A*, 674, 299–307.

Rafi, H.K., Pal, D., Patil, N., Starr, T.L., Stucker, B.E. (2014). Microstructure and Mechanical Behavior of 17-4 Precipitation Hardenable Steel Processed by Selective Laser Melting. *Journal of Materials Engineering and Performance*, 23(12), 4421–4428.

Ramsperger, M., Singer, R.F., Körner, C. (2016). Microstructure of the Nickel-Base Superalloy CMSX-4 Fabricated by Selective Electron Beam Melting. *Metallurgical and Materials Transactions A*, 47(3), 1469–1480.

Ravnikar, D., Dahotre, N.B., Grum, J. (2013). Laser coating of aluminum alloy EN AW 6082-T651 with TiB2 and TiC: Microstructure and mechanical properties. *Applied Surface Science*, 282, 914–922.

Rosenthal, D. (1946). The theory of Moving Sources of Heat and Its Application to Metal Treatments. *Transactions of the A.S.M.E*, 68, 849–865.

Royer, F. (2014). Fonctionnement et singularités du procédé de fusion laser sélective : illustration par application à deux superalliages à base nickel et considérations énergétiques. Thèse de doctorat, École nationale supérieure des Mines de Paris, Paris.

Ryan, E.M., Sabin, T.J., Watts, J.F., Whiting, M.J. (2018). The influence of build parameters and wire batch on porosity of wire and arc additive manufactured aluminium alloy 2319. *Journal of Materials Processing Technology*, 262, 577–584.

Scipioni Bertoli, U., Wolfer, A.J., Matthews, M.J., Delplanque, J.-P.R., Schoenung, J.M. (2017). On the limitations of Volumetric Energy Density as a design parameter for Selective Laser Melting. *Materials & Design*, 113, 331–340.

Senninger, O., Gandin, C.-A., Guillemot, G. (2018). Modeling of eutectic growth kinetics with thermodynamic couplings. *Acta Materialia*, 161, 110–126.

Simonelli, M., Tse, Y.Y., Tuck, C. (2012). Microstructure of Ti-6Al-4V produced by selective laser melting. *Journal of Physics: Conference Series*, 371, 012084.

Spierings, A.B., Dawson, K., Heeling, T., Uggowitzer, P.J., Schäublin, R., Palm, F., Wegener, K. (2017). Microstructural features of Sc- and Zr-modified Al-Mg alloys processed by selective laser melting. *Materials & Design*, 115, 52–63.

Spierings, A.B., Dawson, K., Dumitraschkewitz, P., Pogatscher, S., Wegener, K. (2018). Microstructure characterization of SLM-processed Al-Mg-Sc-Zr alloy in the heat treated and HIPed condition. *Additive Manufacturing*, 20, 173–181.

Sun, Z., Tan, X., Tor, S.B., Yeong, W.Y. (2016). Selective laser melting of stainless steel 316L with low porosity and high build rates. *Materials & Design*, 104, 197–204.

Takata, N., Kodaira, H., Sekizawa, K., Suzuki, A., Kobashi, M. (2017). Change in microstructure of selectively laser melted AlSi10Mg alloy with heat treatments. *Materials Science and Engineering: A*, 704, 218–228.

Thijs, L., Kempen, K., Kruth, J.-P., Van Humbeeck, J. (2013). Fine-structured aluminium products with controllable texture by selective laser melting of pre-alloyed AlSi10Mg powder. *Acta Materialia*, 61(5), 1809–1819.

Tourret, D., Reinhart, G., Gandin, C.-A., Iles, G.N., Dahlborg, U., Calvo-Dahlborg, M., Bao, C.M. (2011). Gas atomization of Al–Ni powders: Solidification modeling and neutron diffraction analysis. *Acta Materialia*, 59(17), 6658–6669.

Turnbull, D. (1962). On the relation between crystallization rate and liquid structure. *The Journal of Physical Chemistry*, 66(4), 609–613.

Vandyoussefi, M., Kerr, H.W., Kurz, W. (2000). Two-phase growth in peritectic Fe–Ni alloys. *Acta Materialia*, 48(9), 2297–2306.

Vinson, P. (2015). Fusion sélective par laser de lits de poudre : étude sur le recyclage de la poudre et détection de défauts au cours de la fabrication par imagerie thermi-que. Thèse de doctorat, Mines Paris Tech, Paris.

Wang, H., Zhang, X., Wang, G.B., Shen, J., Zhang, G.Q., Li, Y.P., Yan, M. (2019). Selective laser melting of the hard-to-weld IN738LC superalloy: Efforts to mitigate defects and the resultant microstructural and mechanical properties. *Journal of Alloys and Compounds*, 807, 151662.

Wang, N., Mokadem, S., Rappaz, M., Kurz, W. (2004). Solidification cracking of superalloy single- and bi-crystals. *Acta Materialia*, 52(11), 3173–3182.

Wang, Y.M., Voisin, T., McKeown, J.T., Ye, J., Calta, N.P., Li, Z., Zeng, Z., Zhang, Y., Chen, W., Roehling, T.T., Ott, R.T., Santala, M.K., Depond, P.J., Matthews, M.J., Hamza, A.V., Zhu, T. (2018). Additively manufactured hierarchical stainless steels with high strength and ductility. *Nature Materials*, 17(1), 63–71.

Wu, J., Wang, X.Q., Wang, W., Attallah, M.M., Loretto, M.H. (2016). Microstructure and strength of selectively laser melted AlSi10Mg. *Acta Materialia*, 117, 311–320.

Yu, G., Gu, D., Dai, D., Xia, M., Ma, C., Shi, Q. (2016). On the role of processing parameters in thermal behavior, surface morphology and accuracy during laser 3D printing of aluminum alloy. *Journal of Physics D: Applied Physics*, 49(13), 135501.

Zhang, F., Levine, L.E., Allen, A.J., Campbell, C.E., Lass, E.A., Cheruvathur, S., Stoudt, M.R., Williams, M.E., Idell, Y. (2017a). Homogenization kinetics of a nickel-based superalloy produced by powder bed fusion laser sintering. *Scripta Materialia*, 131, 98–102.

Zhang, H., Zhu, H., Nie, X., Yin, J., Hu, Z., Zeng, X. (2017b). Effect of Zirconium addition on crack, microstructure and mechanical behavior of selective laser melted Al-Cu-Mg alloy. *Scripta Materialia*, 134, 6–10.

Zhao, L., Santos Macías, J.G., Ding, L., Idrissi, H., Simar, A. (2019). Damage mechanisms in selective laser melted AlSi10Mg under as built and different post-treatment conditions. *Materials Science and Engineering: A*, 764, 138210.

Zhou, L., Mehta, A., Schulz, E., McWilliams, B., Cho, K., Sohn, Y. (2018). Microstructure, precipitates and hardness of selectively laser melted AlSi10Mg alloy before and after heat treatment. *Materials Characterization*, 143, 5–17.

Zimmermann, M. (1990). Solidification rapide de l'eutectique Al-Al2Cu par refusion laser. Thèse de doctorat, EPFL, Lausanne.